ACS APPLIED MATERIALS & INTERFACES

www.acsami.org

Research Article

Effect of the Substrate on MoS_2 Monolayer Morphology: An Integrated Computational and Experimental Study

Shiddartha Paul, Riccardo Torsi, Joshua A. Robinson, and Kasra Momeni*

Cite This: *ACS Appl. Mater. Interfaces* 2022, 14, 18835−18844

Read Online

ACCESS | Metrics & More | Article Recommendations | Supporting Information

ABSTRACT: Synthesis of two-dimensional materials, specifically transition metal dichalcogenides (TMDs), with controlled lattice orientations is a major barrier to their industrial applications. Controlling the orientation of as-grown TMDs is critical for preventing the formation of grain boundaries, thus reaching their maximum mechanical and optoelectronic performance. Here, we investigated the role of the substrate's crystallinity in the growth orientation of 2D materials using reactive molecular dynamics (MD) simulations and verified with experimental growth using the chemical vapor deposition (CVD) technique. We considered MoS_2 as our model material and investigated its growth on crystalline and amorphous silica and sapphire substrates. We revealed the role of the substrate's energy landscape on the orientation of as-grown TMDs, where the presence of monolayer−substrate energy barriers perpendicular to the streamlines hinder the detachment of precursor nuclei from the substrate. We show that MoS_2 monolayers with controlled orientations could not be grown on the SiO_2 substrate and revealed that amorphization of the substrate changes the intensity and equilibrium distance of monolayer−substrate interactions. Our simulations indicate that 0° rotated MoS_2 is the most favorable configuration on a sapphire substrate, consistent with our experimental results. The experimentally validated computational results and insight presented in this study pave the way for the high-quality synthesis of TMDs for high-performance electronic and optoelectronic devices.

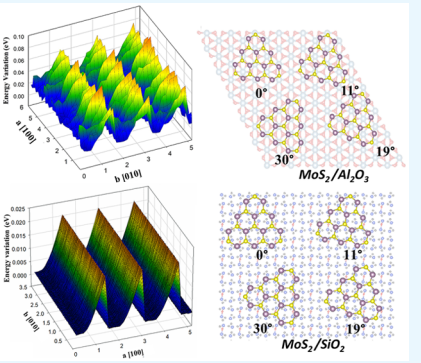

KEYWORDS: *2D materials, substrate effect, molecular dynamics, synthesis, chemical vapor deposition*

1. INTRODUCTION

Atomically thin 2D materials have attracted the research community's attention because of their unique features and potential applications, e.g., solar cells[1,2] and flexible electronics.[3,4] In particular, transition metal dichalcogenides (TMDs) have been widely studied for their optoelectronic applications in next-generation flexible electronic devices. Molybdenum disulfide (MoS_2) has drawn the most attention for its exceptional optoelectronic[5] and electronic properties.[6] Besides the electrical properties, MoS_2 nanomembrane has outstanding thermal stability and mechanical characteristics.[7] MoS_2 shows even more superior electronic and mechanical properties than graphene in some cases. Besides, one of the unique features of MoS_2 is its transition from an indirect to a direct bandgap material upon the formation of single layers.[8] Utilizing these unique properties of MoS_2 on an industrial scale mandates its large-area uniform production, requiring a fundamental understanding of growth mechanisms.[9,10] Uniform CVD-grown monolayer film requires the deposited MoS_2 triangular islands to be in a specific orientation. Some studies reported that the nucleation of monolayer MoS_2 could be guided by the edges of the substrate step to form highly orientated MoS_2 monolayers.[11,12] Here, we have focused on understanding the role of the substrate's crystallinity on the preferred orientation of as-grown MoS_2 monolayers.

Weak van der Waals forces bond bulk MoS_2 layers; thus, it is easy to exfoliate MoS_2 monolayers using Scotch tape[13] or liquid-phase exfoliation.[14] These synthesis processes are known as the top-down methods, where the MoS_2 layers are peeled off by overcoming van der Waals attractions. Mechanically exfoliated semiconductors have been used to construct versatile electronic devices like ultrasensitive photodetectors[15,16] and field-effect transistors[17] with high on/off current ratio memory cells.[18] However, the thickness, crystal quality, and scalability of the synthesized material are not controllable in the exfoliation process.

Recently, bottom-up wafer-scale synthesis processes like CVD and atomic layer deposition (ALD) have been implemented for atomically thin large-area production of MoS_2.[19−21] The reactant gases (precursors) are transported to the substrate surface (reaction zone) by convection and diffusion in the CVD process. Then the product of gaseous reactions deposits on the substrate, forming the 2D monolayer

Received: February 25, 2022
Accepted: April 11, 2022
Published: April 14, 2022

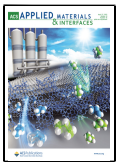

https://doi.org/10.1021/acsami.2c03471
ACS Appl. Mater. Interfaces 2022, 14, 18835−18844

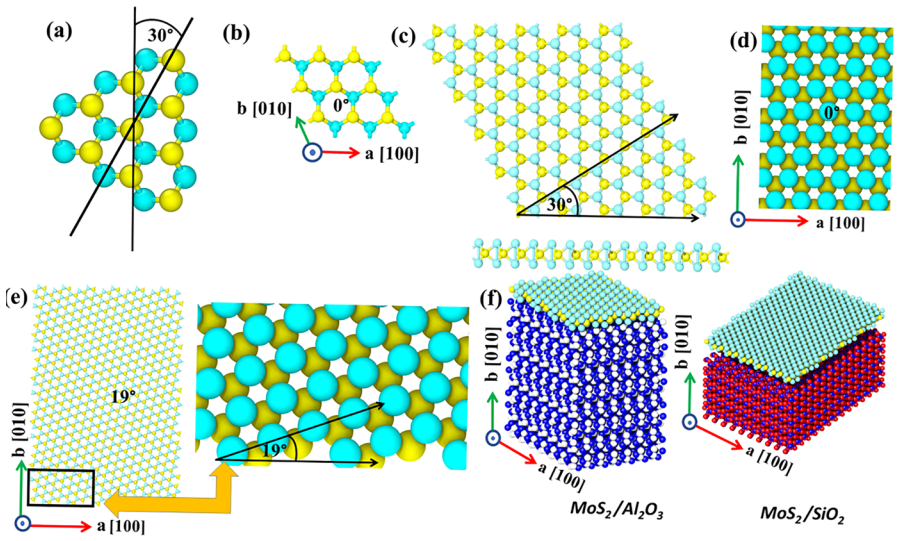

Figure 1. Monolayer MoS_2 structure on different substrates. (a) A standalone MoS_2 triangular island; (b) 0° rotated and (c) 30° rotated MoS_2 structure with minimum mismatch strain for a *c*-plane sapphire (Al_2O_3) substrate; (d) 0° rotated and (e) 19° rotated MoS_2 structure with minimum mismatch strain for a *c*-plane quartz substrate (with enlarged atomic structure illustration); (f) 19° rotated MoS_2/Al_2O_3 and MoS_2/Si_2O_3 simulation structure for the simulation.

material. Various computational methods such as finite element analysis,[22−25] atomistic simulation,[26,27] and the first-principle method[28] have been employed to guide the synthesis of 2D materials.[10,29−31] Although most of these studies focus on first principal/DFT calculations, these simulations cannot analyze larger atomic systems involved in TMDs with certain rotation angles. Thus, in order to understand the mechanisms underlying their growth, other simulation techniques such as molecular dynamics (MD),[32] phase-field,[33,34] or multiscale models[35−37] need to be used.

In this study, we pursued an integrated computational and experimental approach to understand the role of the substrate on the growth morphology of 2D islands. We have used MD simulations to gain insight into the effect of substrate on the orientation of as-grown 2D materials and experimentally synthesized MoS_2 on crystalline and amorphous Al_2O_3 and SiO_2 substrates to verify our predictions. In particular, we studied the effect of substrate amorphization on the growth orientation, MoS_2/substrate bonding strength, and the energy landscape of differently oriented MoS_2 monolayers. The computational results with experimental benchmarking presented here pave the way to the controlled synthesis of MoS_2 monolayers.

2. MATERIALS AND METHODS

2.1. Reactive Molecular Dynamics Model. The reported experimental observations dictate that the distribution and orientation of MoS_2 triangles are strong functions of the substrates.[25,38,39] The MoS_2 triangular islands synthesized on SiO_2 substrates are arbitrarily oriented,[25,40] while those on sapphire substrates have preferred 0° and 60° orientations. The uniform orientation distribution of MoS_2 triangular islands largely depends on the interaction between the as-grown 2D materials with the substrate. This interaction determines the islands' size and orientation by influencing the nucleation process and driving forces of growth. We use reactive MD to investigate the effect of the substrate, including amorphization, on the orientation and bonding of as-grown MoS_2 islands. We further verify our computational predictions by comparing them with the experimental growth of MoS_2 monolayers (see Section 4).

We prepared MoS_2 structures with various orientations on crystalline and amorphous Al_2O_3 and SiO_2 substrates. Figure 1a shows a standalone 30° rotated MoS_2 triangular island, and Figure 1b shows the 0° oriented MoS_2 supercell for placing on an Al_2O_3 substrate. The MoS_2 structure rotated by 30° with respect to the *c*-axis of the Al_2O_3 substrate is shown in Figure 1c. The orientation angle dictates the size of the unit cell by mandating minimization of the mismatch strain between the substrate and as-grown 2D material (see the Supporting Information for details). We have chosen these orientation angles to have computationally tractable simulation cell sizes. For a supercell of rotated MoS_2 designated as (a_{rot}, b_{rot}) and a supercell of the substrate designated as (a_{sub}, b_{sub}), the mismatch strain will be minimum when $|a_{rot} - a_{sub}|$ and $|b_{rot} - b_{sub}|$ vanish. Considering the discrete nature of the crystal structures, this difference will be minimum when the reminder of ua_{sub}/a_{rot} and vb_{sub}/b_{rot} are minimum, where u and v are integer numbers. Values of $mod(ua_{sub}/a_{rot})$ and $mod(vb_{sub}/b_{rot})$, where *mod* represents the modulo operator, corresponding to the mismatch strains between the rotated monolayer and substrate.

Dimensions of MoS_2, Al_2O_3, and SiO_2 unit cells are given in Table S1 of the Supporting Information. The number of unit cells used for the Al_2O_3 substrate for different rotated MoS_2 islands is in Table S2 of the Supporting Information. Moreover, the dimensions of the strained MoS_2 monolayers on the Al_2O_3 substrate are shown in Table S3 of the Supporting Information. The hexagonal MoS_2 structures are trimmed to make a tetragonal unit cell with unit vectors along the **a**-[001] and **b**-[010] crystalline directions, minimizing the mismatch strain following the fundamental theoretical methodology explained. Figure 1d,e shows rotated MoS_2 structures at 0° and 19° on the SiO_2 substrate. The dimensions of the trimmed tetragonal-shaped MoS_2 unit cells are given in Table S4 of the Supporting Information. The corresponding supercell dimensions of the SiO_2 substrate are shown in Table S5 of the Supporting Information. The MoS_2 supercell is strained to

https://doi.org/10.1021/acsami.2c03471
ACS Appl. Mater. Interfaces 2022, 14, 18835−18844

match the SiO_2 supercell's dimensions. Dimensions of rotated MoS_2 monolayers on SiO_2 substrate are given in Table S6 of the Supporting Information. The complete structure of 19° MoS_2 on different substrates is presented in Figure 1f.

Mismatch strain along each lattice vector is shown in Figure 2 as a function of the number of unit cells in a supercell for a

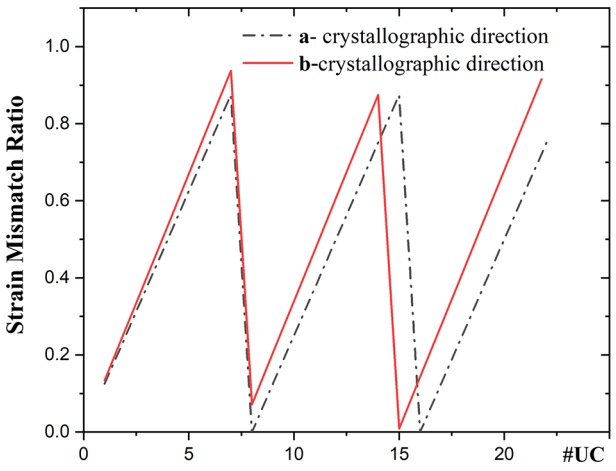

Figure 2. Mismatch strain versus the number of sapphire unit cells for a MoS_2 monolayer rotated by 30°. The results indicate a periodic variation of the mismatch strain versus the number of substrate unit cells. The number of unit cells in the supercell is chosen as the minimum value of u and v, which minimizes the mismatch.

30° MoS_2 on a c-plane of the sapphire substrate. The supercell size is determined as the least number of unit cells with a minimum mismatch between the substrate and the 2D material. The crystal structure for the MD simulations is considered periodic in-plane of the substrate. We have built the simulation cell by stretching the MoS_2 supercell to match the supercell of the substrate. The results reveal the periodic variation of the mismatch strain versus the number of unit cells in a supercell. We have calculated the bonding strength of MoS_2 on amorphous Al_2O_3 and SiO_2 substrates, where we considered 10 different amorphous Al_2O_3 and SiO_2 structures for each rotated MoS_2 structure to ensure a statistically representative conclusion. These substrates were created by assigning 10 different initial velocities to the substrates' atoms during the amorphization process.

2.2. Computational Methodology. We utilized a reactive empirical bond order (REBO) potential[41] to model the Mo−S interaction. This REBO potential can capture the formation and breaking of chemical bonds. The interaction energy for REBO potential is[42]

$$E_b = \frac{1}{2}\sum_{i\neq j} f_{ij}^{c}(r_{ij})\left[\left(1+\frac{Q_{ij}}{r_{ij}}\right)Ae^{-\alpha r_{ij}} - b_{ij}Be^{-\beta r_{ij}}\right] \quad (1)$$

Here, E_b is the binding energy, $f_{ij}^{c}(r_{ij})$ is the cutoff function, b_{ij} is the bond order potential and r_{ij} is the interatomic distance between atoms i and j. Also, Q, α, and β are geometrical functions dependent on the equilibrium distance between atoms i and j. A and B are the attractive and repulsive energy-related terms, respectively.

We have considered both amorphous and crystalline forms of Al_2O_3 and SiO_2 substrates. To model the Al−O interaction, we use COMB3 potential.[43] The COMB3 potential has capabilities crucial for accurately modeling the physical phenomena involved during the growth of MoS_2, e.g., the formation and breaking of bonds and Coulombic interactions for various elements. To define the interatomic interaction between the Si−O, we have used the Tersoff potential[44,45] with parameters presented in ref 46. The van der Waals interactions between the MoS_2 monolayer and Al_2O_3 and SiO_2 substrates are modeled with the Lennard-Jones (LJ) potential with the interaction parameters given in Table 1. We have used 8.5 Å as a cutoff distance for those LJ interactions, which is more than two times the LJ equilibrium distances involved.

Table 1. List of σ (Å) and ε (eV) Values of the LJ Interactions for Different Substrates

elements	σ (Å)	ε (eV)
Mo−Al[47]	2.57	0.00585
S−Al[48]	2.23	0.00889
Mo−O[49]	2.93	0.004
S−O[49]	3.37	0.00884
Mo−Si[49]	3.27	0.00562
Si−S[49]	3.71	0.00562

2.2.1. Amorphous Al_2O_3 Substrate. Amorphous alumina (Al_2O_3) has been prepared by melting the crystal structure and quenching it to room temperature. We start with a triclinic crystalline Al_2O_3, heated to 3000 K in the *NVT* ensemble with a time step of 1.8 fs for 81 ps,[50] then cooling at 300 K using the temperature rescaling method of 90 ps and *NVE* equilibration for 63 ps. Then the structure was further brought down to 0 K for 10 ps with a time step of 1 fs. We repeated this process to get 10 different structures for 10 different initial velocities of the atoms.

2.2.2. Amorphous SiO_2 Substrate. Amorphous SiO_2 (a-SiO_2) is prepared using the same melt-quench procedure we use to prepare amorphous Al_2O_3. We start from a crystalline SiO_2 structure with periodic boundary conditions applied in all directions. The system was heated to 5000 K with an *NVT* ensemble for 7.5 ps,[51] then cooled to 300 K with a cooling rate of 10^{12} K/s to maintain the computational efficiency. Then we relaxed the system under the *NVE* ensemble for 15 ps without any disturbance for energy stabilization. We have repeated this process to get 10 different structures for 10 different initial velocities of the atom.

2.2.3. MoS_2−Substrate Energy Landscape. For mapping interaction energy between MoS_2 and the substrate, we have relaxed the whole structure (MoS_2 on top of the substrate) for 20 ps at 0 K under the *NVE* ensemble. After the relaxation, we scan the MoS_2 monolayer over the substrate and calculate the energy landscape. To do this, we have moved the MoS_2 by 0.138 Å (1/20 of the Mo−Mo bond length) in the b-crystallographic direction, i.e., [010], followed by moving it 1.58 Å (1/20 of the Mo−S bond length) in the a-crystallographic direction, i.e., [100], in each step[52] to capture the detailed interaction with each bond. For the SiO_2, we have relaxed the whole structure (MoS_2 on the top of the SiO_2 substrate) for 20 ps and followed the same algorithm we used for Al_2O_3. In this case, we move the MoS_2 monolayer along the a-[100] and b-[010] crystallography directions of SiO_2 with steps of 0.138 Å (1/20 of the Mo−Mo bond length) and by 0.074 Å (1/20 of the Si−O bond length), respectively.

MoS_2−Substrate Binding Energy. Initially, we place the MoS_2 monolayer structure at a distance of 15 Å from the substrate. Using the *NVE* ensemble, we relaxed the whole

https://doi.org/10.1021/acsami.2c03471
ACS Appl. Mater. Interfaces 2022, 14, 18835−18844

structure (MoS_2 on the top of the substrate) for 40 ps at 0 K. We then move the MoS_2 toward the substrate at a velocity of 0.44 Å/ps to capture MoS_2–substrate interaction energy with high resolution.

2.3. MOCVD MoS_2 Film Synthesis. MoS_2 films are synthesized in a horizontal, hot-wall metal–organic chemical vapor deposition (MOCVD) system to verify the computational predictions. The sulfur source is a 500 mL H_2S (99.5%, Sigma-Aldrich) lecture bottle with an outlet pressure of 30 psi. A mass flow controller mounted after the lecture bottle regulates the H_2S flux to the substrate. H_2S is preferred over other commonly used sulfur precursors like diethyl sulfide because chalcogen-hydride gases have been shown to yield higher quality TMD films in terms of both morphology and impurity concentration.[53,54] Furthermore, the carbon-containing chalcogen precursor has been shown to form graphitic carbon on the substrate surface, which impedes the study of substrate effects on TMD growth.[54] Although H_2S is a favorable precursor for MOCVD growth of MoS_2, it is also highly toxic. Because of this, safety valves and gas detectors are mounted to the MOCVD system to prevent and identify any possible leaks during operation. $Mo(CO)_6$ (99.9%, Sigma-Aldrich), the Mo source, is loaded in a temperature and pressure-controlled stainless steel bubbler. $Mo(CO)_6$ is chosen as the metal–organic precursor because of its clean decomposition mechanism and its high vapor pressure.[55] The pressure inside the $Mo(CO)_6$ bubbler is kept constant at 735 Torr, and the temperature is maintained at 24 °C. A controlled amount of H_2 is flown through the bubbler as the carrier gas to precisely regulate the amount of $Mo(CO)_6$ delivered to the substrate during synthesis. Substrates are placed on an alumina crucible loaded in the center of the furnace's hot zone to commence film growth.

Before flowing precursors, the furnace is pumped down to its base pressure of 20 mTorr and maintained at 300 °C to drive off moisture. After this soak, the system pressure is raised to a growth pressure of 50 Torr by flowing 2 standard liters per minute of Ar, which acts as the main carrier gas to push precursors down the tube, effectively maintaining a laminar flow and ensuring even deposition. Once the growth pressure was reached, we ramped up the furnace's temperature to the growth temperature at a rate of 50 °C/min (Figure S1 in Supporting Information). The standard growth temperature to grow monolayer MoS_2 films is 900 °C. However, both SiO_2 and ALD Al_2O_3 react with H_2S at these conditions, effectively restricting the growth temperature on these substrates. It has been shown that sulfur can etch the silicon substrate, leaving behind ultrathin freestanding silica.[56] Conversely, ALD Al_2O_3 reacts with H_2S to form interfacial AlS_x. To address substrate stability concerns, the synthesis temperature is 900 °C for growths on sapphire and quartz, and it is lowered to 700 and 450 °C for ALD Al_2O_3 and SiO_2, respectively. Ten sccm H_2S is flown in the chamber and is maintained throughout the synthesis process. We also grow MoS_2 monolayers using the powder vapor transport (PVT) technique on ALD Al_2O_3 and SiO_2 with a growth temperature of 800 °C (Figure S2 in the Supporting Information). Although the size of monolayer islands is larger in the latter case, the orientation and morphology of the islands are yet comparable to what has been grown by the MOCVD technique at lower temperatures.

Previous studies indicate that temperature only plays a weak role in determining the growth orientation.[9,25,30,34,37,57] Temperature variation mainly affects the diffusion coefficient of precursors, buoyancy forces, and nucleation rate of the monolayers. The attachment rate will be higher at lower temperatures, increasing nucleation density.[58,59] Furthermore, the adatom diffusion rate on the substrate surface will be lower, effectively decreasing grain size at lower growth temperatures.[58,59] The morphology (not orientation) of the monolayer MoS_2 is also determined by the Mo/S ratio and the anisotropy of edge and surface diffusion coefficients.[9,60] Thus, although we used different synthesis temperatures for MOCVD growth on each substrate to avoid the initiation of undesirable chemical reactions, such variations shall not affect our conclusions regarding the effect of the substrate on the orientation of as-grown MoS_2 monolayers.

H_2 gas at a rate of 7.5 sccm is flown through the $Mo(CO)_6$ bubbler for the first 2 min of the film growth. This nucleation step creates metal-rich nuclei on the substrate surface, forming a template for subsequent film growth. The metal-rich nuclei are then ripened by ceasing $Mo(CO)_6$ and maintaining H_2S flow for 10 min. Lateral growth leading to coalescence is achieved by reintroducing the metal precursor at half the nucleation flow to prevent the formation of additional nuclei. A postgrowth anneal under H_2S flow is used to reduce the number of metal-rich particles on the surface and the density of sulfur vacancies resulting from the growth process.[53] The system is then fan cooled down to room temperature.

Atomic force microscopy (AFM) is employed to investigate the MoS_2 film morphology on different growth substrates. The micrographs are obtained using the Bruker Dimension Icon instrument equipped with a ScanAsyst-Air (k = 0.4 N/m) tip. The AFM tool is used in PeakForce Tapping mode to ensure appropriate image resolution while avoiding film damage. To obtain high-quality micrographs, the tip scan rate is set at 0.5 Hz while maintaining a peak force set point of 1.00 nN and a peak force frequency of 2 kHz.

Our experimental measurements indicate the formation of MoS_2 islands with preferred orientations on sapphire (Figure 3 and Figure S2) while they are randomly oriented on quartz, amorphous Al_2O_3, and SiO_2 structures (Figure 3 and Figure S2). The MoS_2 islands grown on sapphire form triangles with sharp edges with 0 and 60° growth orientations leading to a

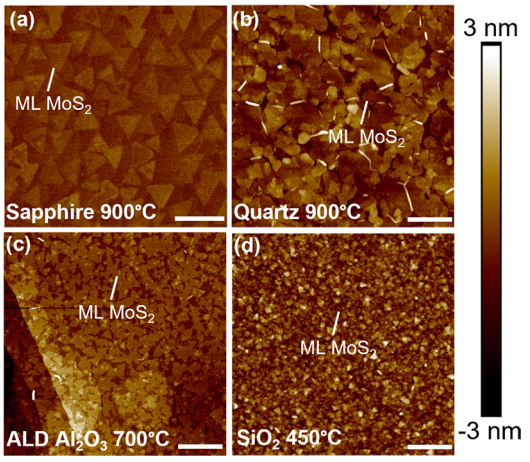

Figure 3. Atomic force microscopy scans of MOCVD-grown monolayer MoS_2. Monolayers are grown on (a) c-plane sapphire, (b) quartz, (c) amorphous Al_2O_3, and (d) amorphous SiO_2. The arrows indicate regions of monolayer MoS_2 on top of each substrate. The scale bars are 400 nm.

https://doi.org/10.1021/acsami.2c03471
ACS Appl. Mater. Interfaces 2022, 14, 18835–18844

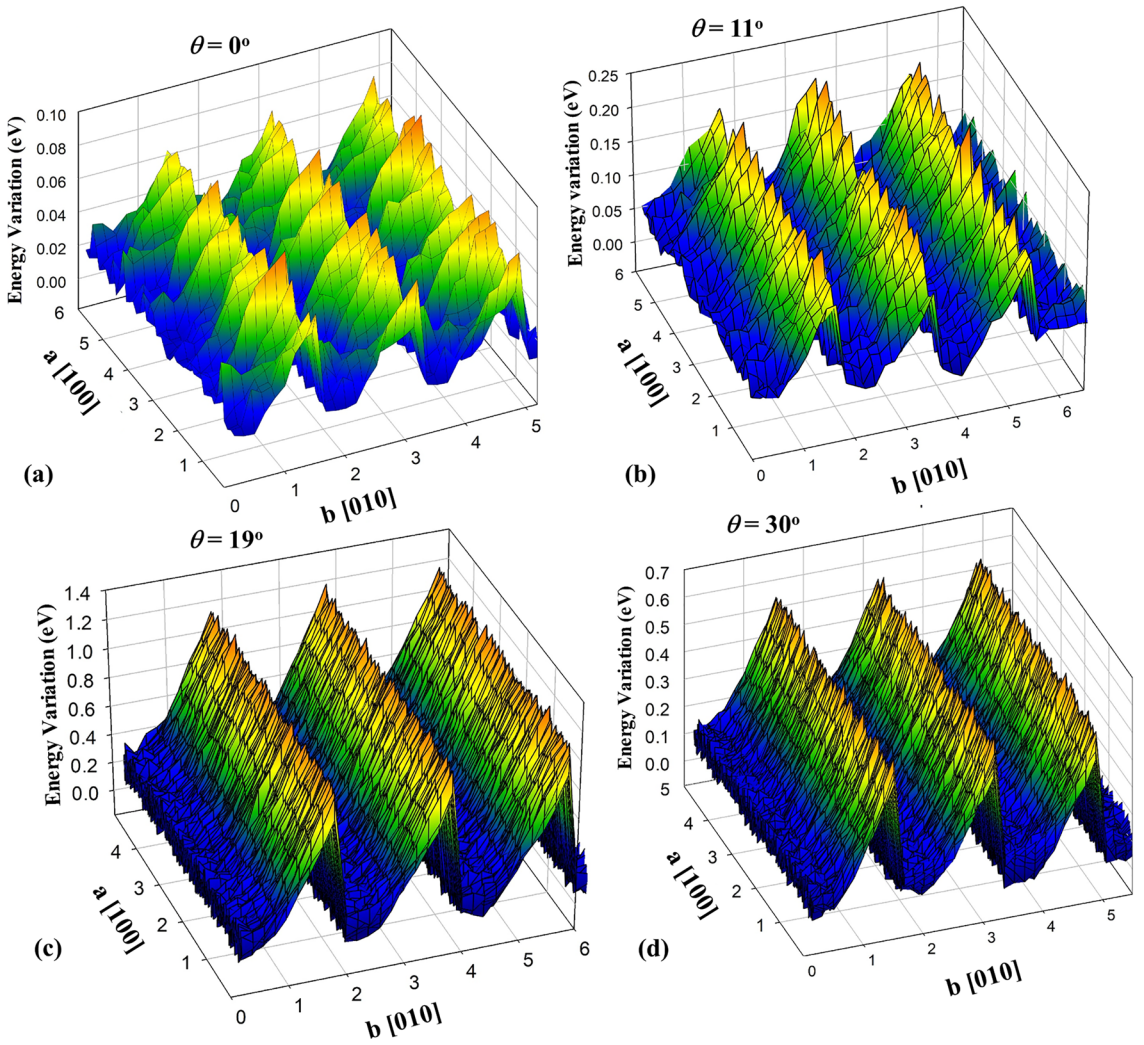

Figure 4. Energy mapping of differently oriented MoS_2 monolayers on a crystalline sapphire substrate. (a) 0°, (b) 11°, (c) 19°, and (d) 30° rotated MoS_2. The minimum energy in each case is considered to be zero.

uniform monolayer film upon coalescence (Figure S3), while the ones grown on quartz do not show any orientation preference and have rounded edges. The latter results are surprising as a preferred growth on crystalline SiO_2 (quartz) substrate is speculated. However, this is consistent with our MD simulations indicating no egg-shell type energy landscape between MoS_2 monolayer and quartz substrate. This edge geometry could be explained by the potential lower edge-to-surface diffusion ratio of precursors on the quartz substrate than on the sapphire substrate.[9,61] For the MoS_2 islands grown on quartz, occasionally, out of plane growth of 2D fins is observed where two islands meet. The smaller MOCVD-grown islands on the amorphous SiO_2 substrate are associated with the lower growth temperature and thus smaller critical nucleus size and higher nucleation rate. Larger MoS_2 monolayers were grown on the same amorphous substrate using the PVT technique with a higher growth temperature of 800 °C (Figure S2 in the Supporting Information).

3. RESULTS AND DISCUSSION

The MoS_2 monolayer and crystalline Al_2O_3 (sapphire) have a 3-fold symmetry, where the rotation angle $\theta = \Theta$ is conjugate to $\theta = \Theta + 60°$, and total energy $E(\Theta) = E(-\Theta)$.[62,63] Therefore, we considered rotation angles between $\theta \in [0°, 30°]$. Here, we considered crystalline and amorphous forms of Al_2O_3 and SiO_2 substrates and calculated the surface energy landscape of differently oriented MoS_2 monolayers on these substrates. Our results have a major implication for the growth of MoS_2 monolayers in horizontal growth chambers. The results imply that the final morphology of the MoS_2 is determined by the location of the substrate in the growth chamber[9,10,25] and by the crystallography orientation of the substrate with respect to the streamline.

3.1. Sapphire Substrate. Figure 4 shows the energy landscape of MoS_2 on a sapphire (crystalline Al_2O_3) substrate. These results indicate that 0° oriented MoS_2 forms an energy landscape with the largest variation along the *a*-axis. Thus, the 0° MoS_2 monolayer will be locked in the position where it nucleates. The variations in the *a*-axis will be minimal as the rotation angle reaches 30°. Thus, there will be no substrate interlocking in this direction, and the as-grown monolayers will shear on the substrate upon applying a small force in the [100] direction.

Our results indicate that the energy barrier for the motion of the substrate along the [010] direction increases and then decreases as the MoS_2 rotation angle increases. Among different orientation angles, the 19° MoS_2 has the largest

https://doi.org/10.1021/acsami.2c03471
ACS Appl. Mater. Interfaces 2022, 14, 18835−18844

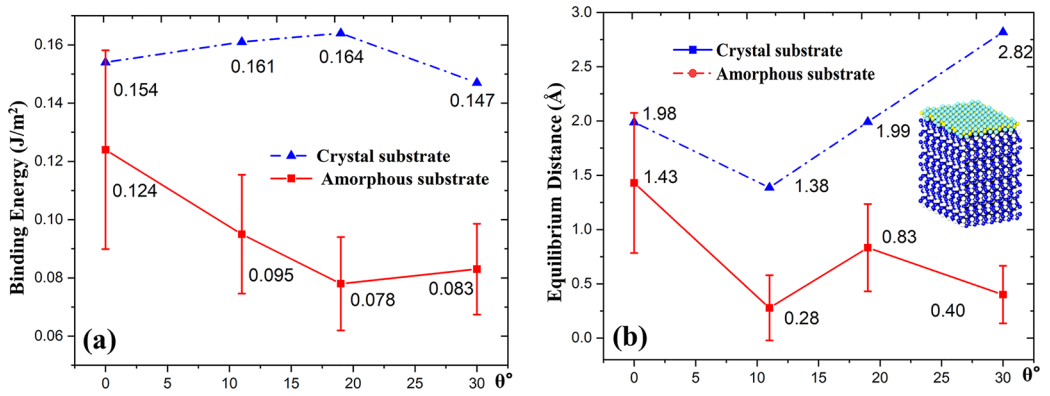

Figure 5. Interaction between MoS_2 monolayer and sapphire substrates. (a) The binding energy and (b) equilibrium distance vs orientation angle of MoS_2 monolayers on the crystalline and amorphous sapphire substrates.

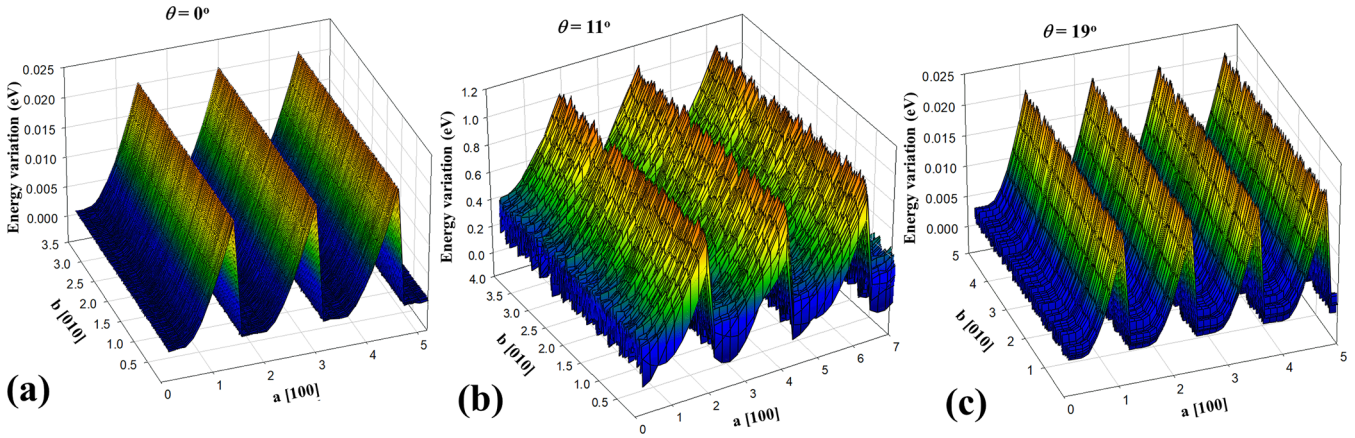

Figure 6. Energy mapping of differently oriented MoS_2 monolayers on the crystalline silica substrate. (a) 0°, (b) 11°, and (c) 19° rotated MoS_2. The energy variations are measured considering the minimum energy to be zero.

energy barrier height and the maximum resistance to motion in the [010] direction. The low interaction energy indicates weak van der Waals attractions that allow the MoS_2 islands to rotate and translate to freely align themselves in perfect orientation. Alignment of the islands along the same direction facilitates their coalescence and formation of the large-area MoS_2 films.[64] The minimum energy barrier height is for a MoS_2 monolayer with a 0° orientation angle, making them the prime candidate for forming large-area monolayers.

We also calculated the binding energy and equilibrium distance between differently oriented MoS_2 monolayers on sapphire (see Figure S7 in the Supporting Information) and amorphous Al_2O_3 (see Tables S7–S10 in the Supporting Information) substrates. The results of our calculations are shown in Figure 5. For amorphous Al_2O_3, we determined the binding energy and equilibrium distance for 10 different amorphous substrate structures created using different seed velocities for the amorphization temperature to ensure statistical reliability. Figure 5a shows the binding energy, E_b, versus orientation angle, θ, for both amorphous and crystal substrates. It reveals that the binding energy between MoS_2 and crystalline sapphire increases by increasing the orientation angle up to 19°. In contrast, we see a decreasing trend of binding energy for the amorphous substrate with a rotation angle, reaching its minimum at 19°. We identified a change in the usual pattern at 19°, e.g., the increasing binding energy decreases at 19° for crystal Al_2O_3 substrate, and the decreasing binding energy increases at 19° for amorphous Al_2O_3 substrate.[65] The 3-fold symmetry of MoS_2 can explain this behavior. In the case of the crystalline sapphire substrate, both the substrate and MoS_2 have the same crystalline symmetry, resulting in the same binding energy (considering the numerical errors) for the 0° and 30° MoS_2, Figure 5a.

In contrast, the amorphous substrate lacks the same 3-fold symmetry. Furthermore, the binding energy between the MoS_2 monolayers and the amorphous sapphire substrate is lower than the crystalline one. Thus, monolayer MoS_2 grown on the amorphous substrate can more easily be transferred to other substrates and devices.[66,67] However, as-grown MoS_2 monolayers will not have a preferred growth orientation on amorphous sapphire, resulting in the growth of polycrystalline monolayer films with degraded properties.[68] There may be more metastable orientations between the ones considered here. However, we could not analyze them using MD simulations because the structure size meeting the stringent lattice-matching criteria becomes very large[69−71] for force convergence in ionic relaxation. The larger system size would require more extensive computational resources, prohibiting the implementation of the simulations using available resources.

Figure 5b shows the plot of equilibrium distances as a function of the orientation angle of the MoS_2 triangular island on the substrate. This equilibrium distance between MoS_2 monolayer and crystalline sapphire is at the minimum for the 11° orientation angle and at the maximum for the 30° orientation angle. Thus, the 30° misorientated angle MoS_2

https://doi.org/10.1021/acsami.2c03471
ACS Appl. Mater. Interfaces 2022, 14, 18835−18844

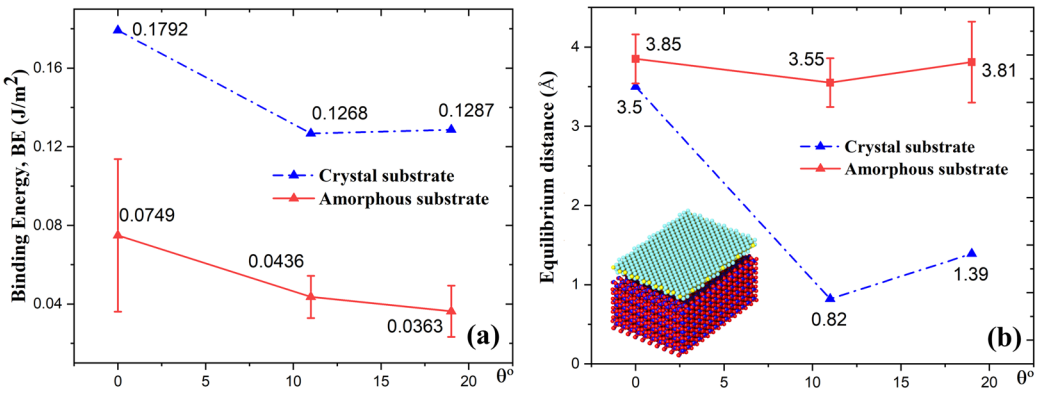

Figure 7. Binding energy and equilibrium distance of differently oriented MoS_2 monolayers on silica substrates. Binding energy (a) and equilibrium distance (b) vs rotational/alignment angle of MoS_2 on the SiO_2 substrates.

monolayers will be the easiest ones to transfer. In the case of amorphous SiO_2 substrates, the maximum equilibrium distance is for the 0° orientation MoS_2, which reduces upon increasing the angle. There is no statistically meaningful difference between the equilibrium distances of MoS_2 islands with orientation angles larger than 0° on the amorphous Al_2O_3 substrates.

3.2. SiO_2 Substrate. Here, we have chosen three different rotated MoS_2 structures for the silica substrate, i.e., 0°, 11°, and 19°. Figure 6 shows the energy landscape of differently oriented MoS_2 monolayers on the crystalline SiO_2 (quartz) substrate. Our results indicate significant energy variation only in the [100] crystallographic direction and the lack of any energy barrier in the [010] crystallography direction for any chosen islands. Thus, the MoS_2 islands forming on crystalline silica substrate are prone to motion upon applying a force along the [010] direction.[72] Furthermore, the maximum energy barrier for the 0° and 19° MoS_2 on a silica substrate positioned at their equilibrium distance is an order of magnitude smaller than the energy barrier of the corresponding rotated MoS_2 monolayers on a sapphire substrate. Therefore, it is easier for the 0° and 19° oriented MoS_2 triangular islands to rotate freely on the silica substrate. In summary, our simulations indicate the lack of any preferred growth orientation similar to the sapphire substrate in a crystalline silica (quartz) substrate. Thus, silica substrate does not offer controlled orientation growth, consistent with our experimental observations (Figure 1b).

We have calculated the binding energy and equilibrium distance of differently oriented MoS_2 islands on the crystalline and amorphous silica substrates (Figure 7). The interaction between a monolayer MoS_2 and crystalline silica has been shown in Figure S8 of the Supporting Information. We prepared 10 different amorphous substrates to have statistically representative data. We included details of our calculations for each of these structures in the Supporting Information (Tables S11−S13).

Figure 7a shows the relationship between the binding energy and orientation angle of MoS_2 monolayers on crystalline and amorphous silica substrates. We revealed a reduction in binding energy, which reaches a plateau as the rotation angle increases. Furthermore, the binding energy is lower for MoS_2 on the amorphous silica substrate compared with the crystalline silica. Although a similar trend is observed for the amorphous silica substrate, making a decisive conclusion is not viable considering the magnitude of the statistical errors. Figure 7b shows the equilibrium distance between the MoS_2 and SiO_2 substrates, indicating its reduction followed by an increase upon increasing of the orientation angle in the case of a quartz substrate. However, the equilibrium distance between MoS_2 islands and amorphous silica is independent of the orientation angle of the MoS_2 islands. We also revealed that the equilibrium distance between MoS_2 monolayers and amorphous silica substrate is higher than crystalline silica, while the binding energy with amorphous silica is lower, in contrast to the Al_2O_3 substrate (Figure 5a). During the simulation, a strong interaction between the SiO_2 substrate and the monolayer MoS_2 was realized, i.e., the MoS_2 structure lost its crystal structure if it was forced to get closer to the substrate than the equilibrium distance. It emphasizes the importance of properly selecting the growing pressure to grow MoS_2 monolayers.

4. CONCLUSIONS

We have studied the role of the substrate on the growth orientation of MoS_2 monolayers to achieve the controlled growth of MoS_2 islands and films. Current simulations provide guidelines about the substrate orientation in a growth chamber concerning the streamlines. The preferred crystallographic orientation of the substrate in a growth chamber is in a direction where the energy barriers of the MoS_2−substrate energy landscape are perpendicular to the streamline's direction, preventing the slide of the as-grown islands on the substrate due to shearing by the carrier gas. We also revealed that the SiO_2 substrate is unsuitable for growing MoS_2 monolayers with constrained orientations. This computational prediction agrees with our experimental observations of MoS_2 monolayers, primarily aligning along the 0° angle on crystalline Al_2O_3 (Figure 3a, Figures S2 and S3 in the Supporting Information).

Our findings demonstrated that amorphization of the substrate could adjust the monolayer−substrate interaction intensity and equilibrium distance, which determine the adhesion of monolayers to the substrate and thus their transfer process. We show that the symmetry of the substrate and monolayer structures substantially affects the binding energy and the equilibrium distance. We also found that the equilibrium distance of MoS_2 on sapphire substrate increases by increasing the misorientation angle beyond 11° while the binding energy decreases. We found that the 0° oriented MoS_2 monolayer had an egg-shell energy landscape on the sapphire substrate, demonstrating an interlocking growth configuration

https://doi.org/10.1021/acsami.2c03471
ACS Appl. Mater. Interfaces 2022, 14, 18835−18844

in both crystallographic orientations of the substrate. We also revealed a negligible energy barrier of the MoS_2 on quartz, indicating a lack of a preferred growth orientation consistent with our experimental findings. Moreover, we demonstrated an increase in the equilibrium distance upon amorphization of quartz substrate followed by a reduction in the binding energy, indicating easier peel off of the MoS_2 monolayers grown on the amorphous SiO_2.

We considered a series of discrete orientation angles, but the structures between those discrete pathways remained unexplored. Still, we believe our experimentally validated MD model demonstrates an excellent prediction capability, which plays a crucial role in the controlled synthesis of monolayers. Our findings enlighten the role of the substrate in the growth of MoS_2. The proposed experimentally validated computational findings can pave the way for high-quality large-area MoS_2 synthesis at an industrial scale for electronic and optoelectronic applications.

■ ASSOCIATED CONTENT

Supporting Information

The Supporting Information is available free of charge at https://pubs.acs.org/doi/10.1021/acsami.2c03471.

Additional experimental and simulation details, including photographs of experimental measurements, atomistic structure, and additional calculation results (PDF)

■ AUTHOR INFORMATION

Corresponding Author

Kasra Momeni − *Department of Mechanical Engineering, The University of Alabama, Tuscaloosa, Alabama 35401, United States;* orcid.org/0000-0002-4209-1129; Phone: +1 (205) 348-1079; Email: kmomeni@ua.edu

Authors

Shiddartha Paul − *Department of Mechanical Engineering, The University of Alabama, Tuscaloosa, Alabama 35401, United States;* orcid.org/0000-0003-4306-180X

Riccardo Torsi − *2D Crystal Consortium, The Pennsylvania State University, University Park, Pennsylvania 16802, United States; Department of Materials Science and Engineering, The Pennsylvania State University, University Park, Pennsylvania 16802, United States;* orcid.org/0000-0001-7748-1074

Joshua A. Robinson − *2D Crystal Consortium, The Pennsylvania State University, University Park, Pennsylvania 16802, United States; Department of Materials Science and Engineering, Materials Research Institute, and Center for 2D and Layered Materials, The Pennsylvania State University, University Park, Pennsylvania 16802, United States*

Complete contact information is available at: https://pubs.acs.org/10.1021/acsami.2c03471

Notes

The authors declare no competing financial interest.

■ ACKNOWLEDGMENTS

This project is partly supported by DoE-ARPA-E OPEN (DE-AR0001066), the National Science Foundation 2D Crystal Consortium − Material Innovation Platform (2DCC-MIP) under NSF cooperative agreement DMR-1539916, and the NSF-CAREER under NSF cooperative agreement CBET-2042683. We would like to thank Dr. Susan Sinnott and Dr. Douglas Spearot for helping us with the MoS_2 REBO potential. R.T. and J.A.R. acknowledge funding from NEWLIMITS, a center in nCORE as part of the Semiconductor Research Corporation (SRC) program sponsored by NIST through award number 70NANB17H041.

■ REFERENCES

(1) Lin, S.; Li, X.; Wang, P.; Xu, Z.; Zhang, S.; Zhong, H.; Wu, Z.; Xu, W.; Chen, H. Interface Designed MoS 2/GaAs Heterostructure Solar Cell with Sandwich Stacked Hexagonal Boron Nitride. *Nat. Publ. Gr.* **2015**, *5*, 15103.

(2) Gu, X.; Cui, W.; Li, H.; Wu, Z.; Zeng, Z.; Lee, S.-T.; Zhang, H.; Sun, B. A Solution-Processed Hole Extraction Layer Made from Ultrathin MoS2 Nanosheets for Efficient Organic Solar Cells. *Adv. Energy Mater.* **2013**, *3* (10), 1262−1268.

(3) Cheng, R.; Jiang, S.; Chen, Y.; Liu, Y.; Weiss, N.; Cheng, H.-C.; Wu, H.; Huang, Y.; Duan, X. Few-Layer Molybdenum Disulfide Transistors and Circuits for High-Speed Flexible Electronics. *Nat. Commun.* **2014**, *5* (1), 1−9.

(4) Yoon, J.; Park, W.; Bae, G.-Y.; Kim, Y.; Jang, H. S.; Hyun, Y.; Lim, S. K.; Kahng, Y. H.; Hong, W.-K.; Lee, B. H.; et al. Flexible Electronics: Highly Flexible and Transparent Multilayer MoS2 Transistors with Graphene Electrodes (Small 19/2013). *Small* **2013**, *9* (19), 3185.

(5) Wu, W.; Wang, L.; Yu, R.; Liu, Y.; Wei, S.-H.; Hone, J.; Wang, Z. L. Piezophototronic Effect in Single-Atomic-Layer MoS 2 for Strain-Gated Flexible Optoelectronics. *Adv. Mater.* **2016**, *28* (38), 8463−8468.

(6) Li, T.; Galli, G. Electronic Properties of MoS 2 Nanoparticles. *J. Phys. Chem. C* **2007**, *111* (44), 16192−16196.

(7) Hasanian, M.; Mortazavi, B.; Ostadhossein, A.; Rabczuk, T.; van Duin, A. C. T. Hydrogenation and Defect Formation Control the Strength and Ductility of MoS2 Nanosheets: Reactive Molecular Dynamics Simulation. *Extrem. Mech. Lett.* **2018**, *22*, 157−164.

(8) Splendiani, A.; Sun, L.; Zhang, Y.; Li, T.; Kim, J.; Chim, C.-Y.; Galli, G.; Wang, F. Emerging Photoluminescence in Monolayer MoS 2. *Nano Lett.* **2010**, *10* (4), 1271−1275.

(9) Momeni, K.; Ji, Y.; Zhang, K.; Robinson, J. A.; Chen, L.-Q. Multiscale Framework for Simulation-Guided Growth of 2D Materials. *npj 2D Mater. Appl.* **2018**, *2* (1), 27.

(10) Briggs, N.; Subramanian, S.; Lin, Z.; Li, X.; Zhang, X.; Zhang, K.; Xiao, K.; Geohegan, D.; Wallace, R.; Chen, L.-Q. Q.; Terrones, M.; Ebrahimi, A.; Das, S.; Redwing, J.; Hinkle, C.; Momeni, K.; van Duin, A.; Crespi, V.; Kar, S.; Robinson, J. A. A Roadmap for Electronic Grade 2D Materials. *2D Mater.* **2019**, *6* (2), 022001.

(11) Yang, P.; Zhang, S.; Pan, S.; Tang, B.; Liang, Y.; Zhao, X.; Zhang, Z.; Shi, J.; Huan, Y.; Shi, Y.; Pennycook, S. J.; Ren, Z.; Zhang, G.; Chen, Q.; Zou, X.; Liu, Z.; Zhang, Y. Epitaxial Growth of Centimeter-Scale Single-Crystal MoS2Monolayer on Au(111). *ACS Nano* **2020**, *14* (4), 5036−5045.

(12) Li, J.; Wang, S.; Jiang, Q.; Qian, H.; Hu, S.; Kang, H.; Chen, C.; Zhan, X.; Yu, A.; Zhao, S.; Zhang, Y.; Chen, Z.; Sui, Y.; Qiao, S.; Yu, G.; Peng, S.; Jin, Z.; Liu, X. Single-Crystal MoS2Monolayer Wafer Grown on Au (111) Film Substrates. *Small* **2021**, *17* (30), 2100743.

(13) Wang, H.; Yuan, H.; Hong, S. S.; Li, Y.; Cui, Y. Physical and Chemical Tuning of Two-Dimensional Transition Metal Dichalcogenides. *Chem. Soc. Rev.* **2015**, *44* (9), 2664−2680.

(14) Coleman, J. N.; Lotya, M.; O'Neill, A.; Bergin, S. D.; King, P. J.; Khan, U.; Young, K.; Gaucher, A.; De, S.; Smith, R. J.; Shvets, I. V.; Arora, S. K.; Stanton, G.; Kim, H.-Y.; Lee, K.; Kim, G. T.; Duesberg, G. S.; Hallam, T.; Boland, J. J.; Wang, J. J.; Donegan, J. F.; Grunlan, J. C.; Moriarty, G.; Shmeliov, A.; Nicholls, R. J.; Perkins, J. M.; Grieveson, E. M.; Theuwissen, K.; McComb, D. W.; Nellist, P. D.; Nicolosi, V. Two-Dimensional Nanosheets Produced by Liquid Exfoliation of Layered Materials. *Science (80-.).* **2011**, *331* (6017), 568−571.

(15) Han, S. W.; Kwon, H.; Kim, S. K.; Ryu, S.; Yun, W. S.; Kim, D. H.; Hwang, J. H.; Kang, J.-S.; Baik, J.; Shin, H. J.; Hong, S. C.; et al. Band-Gap Transition Induced by Interlayer van Der Waals Interaction in MoS 2. *Phys. Rev. B* **2011**, *84* (4), 045409.
(16) Wang, X.; Wang, P.; Wang, J.; Hu, W.; Zhou, X.; Guo, N.; Huang, H.; Sun, S.; Shen, H.; Lin, T.; Tang, M.; Liao, L.; Jiang, A.; Sun, J.; Meng, X.; Chen, X.; Lu, W.; Chu, J. Ultrasensitive and Broadband MoS 2 Photodetector Driven by Ferroelectrics. *Adv. Mater.* **2015**, *27* (42), 6575−6581.
(17) Lin, J.; Zhong, J.; Zhong, S.; Li, H.; Zhang, H.; Chen, W. Modulating Electronic Transport Properties of MoS 2 Field Effect Transistor by Surface Overlayers. *Appl. Phys. Lett.* **2013**, *103* (6), 063109.
(18) Bertolazzi, S.; Krasnozhon, D.; Kis, A. Nonvolatile Memory Cells Based on MoS2/Graphene Heterostructures. *ACS Nano* **2013**, *7* (4), 3246−3252.
(19) Lee, Y.; Zhang, X.; Zhang, W.; Chang, M.; Lin, C.; Chang, K.; Yu, Y.; Wang, J. T.; Chang, C.; Li, L.; et al. Synthesis of Large-area MoS2 Atomic Layers with Chemical Vapor Deposition. *Adv. Mater.* **2012**, *24* (17), 2320−2325.
(20) Jurca, T.; Moody, M. J.; Henning, A.; Emery, J. D.; Wang, B.; Tan, J. M.; Lohr, T. L.; Lauhon, L. J.; Marks, T. J. Low-temperature Atomic Layer Deposition of MoS2 Films. *Angew. Chemie Int. Ed.* **2017**, *56* (18), 4991−4995.
(21) Tan, L. K.; Liu, B.; Teng, J. H.; Guo, S.; Low, H. Y.; Loh, K. P. Atomic Layer Deposition of a MoS2 Film. *Nanoscale* **2014**, *6* (18), 10584−10588.
(22) Paul, S.; Motalab, M.; Zubaer, M. A.; Hossain, M. Z. Strain Rate and Curing Condition Effects on the Stress-Strain Behaviour of Epoxy Adhesive Materials. *J. Adhes. Sci. Technol.* **2017**, *31* (16), 1782−1795.
(23) Liu, Z.; Amani, M.; Najmaei, S.; Xu, Q.; Zou, X.; Zhou, W.; Yu, T.; Qiu, C.; Birdwell, A. G.; Crowne, F. J.; Vajtai, R.; Yakobson, B. I.; Xia, Z.; Dubey, M.; Ajayan, P. M.; Lou, J. Strain and Structure Heterogeneity in MoS2 Atomic Layers Grown by Chemical Vapour Deposition. *Nat. Commun.* **2014**, *5* (1), 5246.
(24) Zhang, F.; Wang, Z.; Zheng, K.; Feng, C.; Yao, R.; Tao, L.; Yu, J.; Chen, X. Promoting Crystal Distribution Uniformity Based on the CVD Method with the Aid of Finite Element Methods. *Cryst. Growth Des.* **2020**, *20* (2), 777−782.
(25) Zhang, F.; Momeni, K.; AlSaud, M. A.; Azizi, A.; Hainey, M. F.; Redwing, J. M.; Chen, L.-Q.; Alem, N. Controlled Synthesis of 2D Transition Metal Dichalcogenides: From Vertical to Planar MoS 2. *2D Mater.* **2017**, *4* (2), 025029.
(26) Paul, S.; Momeni, K.; Levitas, V. I. Shear-Induced Diamondization of Multilayer Graphene Structures: A Computational Study. *Carbon N. Y.* **2020**, *167*, 140−147.
(27) Wang, J.; Namburu, R. R.; Dubey, M.; Dongare, A. M. Origins of Ripples in CVD-Grown Few-Layered MoS2 Structures under Applied Strain at Atomic Scales. *Sci. Rep.* **2017**, *7* (1), 40862.
(28) Şar, H.; Özden, A.; Demiroğlu, İ.; Sevik, C.; Perkgoz, N. K.; Ay, F. Long-Term Stability Control of CVD-Grown Monolayer MoS2. *Phys. status solidi (RRL)-Rapid Res. Lett.* **2019**, *13* (7), 1800687.
(29) Paul, S.; Momeni, K. Mechanochemistry of Stable Diamane and Atomically Thin Diamond Films Synthesis from Bi- and Multilayer Graphene: A Computational Study. *J. Phys. Chem. C* **2019**, *123* (25), 15751−15760.
(30) Momeni, K.; Ji, Y.; Wang, Y.; Paul, S.; Neshani, S.; Yilmaz, D. E.; Shin, Y. K.; Zhang, D.; Jiang, J.-W. W.; Park, H. S.; Sinnott, S.; van Duin, A.; Crespi, V.; Chen, L. Q. Multiscale Computational Understanding and Growth of 2D Materials: A Review. *npj Comput. Mater.* **2020**, *6*, 22.
(31) Gao, J.; Xu, Z.; Chen, S.; Bharathi, M. S.; Zhang, Y.-W. Computational Understanding of the Growth of 2D Materials. *Adv. Theory Simulations* **2018**, *1* (11), 1800085.
(32) Liu, J.; Mohan, A.; Kalia, R. K.; Nakano, A.; Nomura, K.; Vashishta, P.; Yao, K.-T. Boltzmann Machine Modeling of Layered MoS2 Synthesis on a Quantum Annealer. *Comput. Mater. Sci.* **2020**, *173*, 109429.
(33) Wu, J.; Hu, Z.; Jin, Z.; Lei, S.; Guo, H.; Chatterjee, K.; Zhang, J.; Yang, Y.; Li, B.; Liu, Y.; Lai, J.; Vajtai, R.; Yakobson, B.; Tang, M.; Lou, J.; Ajayan, P. M. Spiral Growth of SnSe 2 Crystals by Chemical Vapor Deposition. *Adv. Mater. Interfaces* **2016**, *3* (16), 1600383.
(34) Ji, Y.; Momeni, K.; Chen, L.-Q. A Multiscale Insight into the Growth of H-BN: Effect of the Enclosure. *2D Mater.* **2021**, *8* (3), 035033.
(35) Xuan, Y.; Jain, A.; Zafar, S.; Lotfi, R.; Nayir, N.; Wang, Y.; Choudhury, T. H.; Wright, S.; Feraca, J.; Rosenbaum, L.; Redwing, J. M.; Crespi, V.; van Duin, A. C. T. Multi-Scale Modeling of Gas-Phase Reactions in Metal-Organic Chemical Vapor Deposition Growth of WSe2. *J. Cryst. Growth* **2019**, *527*, 125247.
(36) Srolovitz, D. J.; Dandy, D. S.; Butler, J. E.; Battaile, C. C.; Paritosh. The Integrated Multiscale Modeling of Diamond Chemical Vapor Deposition. *JOM* **1997**, *49* (9), 42−47.
(37) Momeni, K.; Ji, Y.; Chen, L.-Q. Computational Synthesis of 2D Materials Grown by Chemical Vapor Deposition. *J. Mater. Res.* **2022**, *37* (1), 114−123.
(38) Wu, D.; Min, T.; Zhou, J.; Li, C.; Ma, G.; Lu, G.; Xia, M.; Gu, Z. Effect of Substrate Symmetry on the Dendrite Morphology of MoS2 Film Synthesized by CVD. *Sci. Rep.* **2017**, *7* (1), 15166.
(39) Chowdhury, T.; Kim, J.; Sadler, E. C.; Li, C.; Lee, S. W.; Jo, K.; Xu, W.; Gracias, D. H.; Drichko, N. V.; Jariwala, D.; Brintlinger, T. H.; Mueller, T.; Park, H.-G.; Kempa, T. J. Substrate-Directed Synthesis of MoS2 Nanocrystals with Tunable Dimensionality and Optical Properties. *Nat. Nanotechnol.* **2020**, *15* (1), 29−34.
(40) Cun, H.; Macha, M.; Kim, H.; Liu, K.; Zhao, Y.; LaGrange, T.; Kis, A.; Radenovic, A. Wafer-Scale MOCVD Growth of Monolayer MoS2 on Sapphire and SiO2. *Nano Res.* **2019**, *12* (10), 2646−2652.
(41) Liang, T.; Phillpot, S. R.; Sinnott, S. B. Parametrization of a Reactive Many-Body Potential for Mo-S Systems. *Phys. Rev. B* **2009**, *79* (24), 245110.
(42) Han, Y.; Li, M.; Jung, G.; Marsalis, M. A.; Qin, Z.; Buehler, M. J.; Li, L.; Muller, D. A. Sub-Nanometre Channels Embedded in Two-Dimensional Materials. *Nat. Mater.* **2018**, *17*, 129−133.
(43) Choudhary, K.; Liang, T.; Chernatynskiy, A.; Phillpot, S. R.; Sinnott, S. B. Charge Optimized Many-Body (COMB) Potential for Al2O3Materials, Interfaces, and Nanostructures. *J. Phys.: Condens. Matter* **2015**, *27* (30), 305004.
(44) Tersoff, J. New Empirical Model for the Structural Properties of Silicon. *Phys. Rev. Lett.* **1986**, *56* (6), 632−635.
(45) Tersoff, J. New Empirical Approach for the Structure and Energy of Covalent Systems. *Phys. Rev. B* **1988**, *37* (12), 6991−7000.
(46) Munetoh, S.; Motooka, T.; Moriguchi, K.; Shintani, A. Interatomic Potential for Si-O Systems Using Tersoff Parameterization. *Comput. Mater. Sci.* **2007**, *39* (2), 334−339.
(47) Filippova, V. P.; Kunavin, S. A.; Pugachev, M. S. Calculation of the Parameters of the Lennard-Jones Potential for Pairs of Identical Atoms Based on the Properties of Solid Substances. *Inorg. Mater. Appl. Res.* **2015**, *6* (1), 1−4.
(48) Al-Matar, A. K.; Rockstraw, D. A. A Generating Equation for Mixing Rules and Two New Mixing Rules for Interatomic Potential Energy Parameters. *J. Comput. Chem.* **2004**, *25* (5), 660−668.
(49) Farahani, H.; Rajabpour, A.; Khanaki, M.; Reyhani, A. Interfacial Thermal Resistance between Few-Layer MoS2 and Silica Substrates: A Molecular Dynamics Study. *Comput. Mater. Sci.* **2018**, *142*, 1−6.
(50) Gutiérrez, G.; Johansson, B. Molecular Dynamics Study of Structural Properties of Amorphous (Formula Presented). *Phys. Rev. B - Condens. Matter Mater. Phys.* **2002**, *65* (10), 1−9.
(51) Chuang, C. Y.; Li, Q.; Leonhardt, D.; Han, S. M.; Sinno, T. Atomistic Analysis of Ge on Amorphous SiO2using an Empirical Interatomic Potential. *Surf. Sci.* **2013**, *609*, 221−229.
(52) Schönfeld, B.; Huang, J. J.; Moss, S. C. Anisotropic Mean-Square Displacements (MSD) in Single-Crystals of 2H-and 3R-MoS2. *Acta Crystallogr. Sect. B Struct. Sci.* **1983**, *39* (4), 404−407.
(53) Lin, Y. C.; Jariwala, B.; Bersch, B. M.; Xu, K.; Nie, Y.; Wang, B.; Eichfeld, S. M.; Zhang, X.; Choudhury, T. H.; Pan, Y.; Addou, R.; Smyth, C. M.; Li, J.; Zhang, K.; Haque, M. A.; Fölsch, S.; Feenstra, R.

https://doi.org/10.1021/acsami.2c03471
ACS Appl. Mater. Interfaces 2022, 14, 18835−18844

M.; Wallace, R. M.; Cho, K.; Fullerton-Shirey, S. K.; Redwing, J. M.; Robinson, J. A. Realizing Large-Scale, Electronic-Grade Two-Dimensional Semiconductors. *ACS Nano* **2018**, *12* (2), 965−975.
(54) Choudhury, T. H.; Simchi, H.; Boichot, R.; Chubarov, M.; Mohney, S. E.; Redwing, J. M. Chalcogen Precursor Effect on Cold-Wall Gas-Source Chemical Vapor Deposition Growth of WS2. *Cryst. Growth Des.* **2018**, *18* (8), 4357−4364.
(55) Ohta, T.; Cicoira, F.; Doppelt, P.; Beitone, L.; Hoffmann, P. Static Vapor Pressure Measurement of Low Volatility Precursors for Molecular Vapor Deposition below Ambient Temperature. *Chem. Vap. Depos.* **2001**, *7* (1), 33−37.
(56) Zhao, R.; Kim, H.; Stapleton, J.; Liu, Z.-K.; Robinson, J. Freestanding Ultra-Thin Silica. *Cite as AIP Adv.* **2020**, *10*, 025126.
(57) Vilá, R. A.; Momeni, K.; Wang, Q.; Bersch, B. M.; Lu, N.; Kim, M. J.; Chen, L. Q.; Robinson, J. A. Bottom-up Synthesis of Vertically Oriented Two-Dimensional Materials. *2D Mater.* **2016**, *3* (4), 041003.
(58) Nie, Y.; Liang, C.; Cha, P.-R.; Colombo, L.; Wallace, R. M.; Cho, K. A Kinetic Monte Carlo Simulation Method of van Der Waals Epitaxy for Atomistic Nucleation-Growth Processes of Transition Metal Dichalcogenides. *Sci. Rep.* **2017**, *7* (1), 2977.
(59) Kozhakhmetov, A.; Torsi, R.; Chen, C. Y.; Robinson, J. A. Scalable Low-Temperature Synthesis of Two-Dimensional Materials beyond Graphene. *J. Phys. Mater.* **2020**, *4* (1), 012001.
(60) Wang, S.; Rong, Y.; Fan, Y.; Pacios, M.; Bhaskaran, H.; He, K.; Warner, J. H. Shape Evolution of Monolayer MoS 2Crystals Grown by Chemical Vapor Deposition. *Chem. Mater.* **2014**, *26* (22), 6371−6379.
(61) Meca, E.; Shenoy, V. B.; Lowengrub, J. Phase-Field Modeling of Two-Dimensional Crystal Growth with Anisotropic Diffusion. *Phys. Rev. E* **2013**, *88* (5), 52409.
(62) Hu, B.; Ago, H.; Ito, Y.; Kawahara, K.; Tsuji, M.; Magome, E.; Sumitani, K.; Mizuta, N.; Ikeda, K. I.; Mizuno, S. Epitaxial Growth of Large-Area Single-Layer Graphene over Cu(1 1 1)/Sapphire by Atmospheric Pressure CVD. *Carbon N. Y.* **2012**, *50* (1), 57−65.
(63) Ma, Z.; Wang, S.; Deng, Q.; Hou, Z.; Zhou, X.; Li, X.; Cui, F.; Si, H.; Zhai, T.; Xu, H. Epitaxial Growth of Rectangle Shape MoS2 with Highly Aligned Orientation on Twofold Symmetry A-Plane Sapphire. *Small* **2020**, *16*, 2000596.
(64) Dumcenco, D.; Ovchinnikov, D.; Marinov, K.; Lazić, P.; Gibertini, M.; Marzari, N.; Sanchez, O. L.; Kung, Y.-C.; Krasnozhon, D.; Chen, M.-W.; Bertolazzi, S.; Gillet, P.; Fontcuberta I Morral, A.; Radenovic, A.; Kis, A. Large-Area Epitaxial Monolayer MoS2. *ACS Nano* **2015**, *9* (4), 4611−4620.
(65) Ji, Q.; Kan, M.; Zhang, Y.; Guo, Y.; Ma, D.; Shi, J.; Sun, Q.; Chen, Q.; Zhang, Y.; Liu, Z. Unravelling Orientation Distribution and Merging Behavior of Monolayer MoS2 Domains on Sapphire. *Nano Lett.* **2015**, *15* (1), 198−205.
(66) Salvatore, G. A.; Münzenrieder, N.; Barraud, C.; Petti, L.; Zysset, C.; Büthe, L.; Ensslin, K.; Tröster, G. Fabrication and Transfer of Flexible Few-Layers MoS2 Thin Film Transistors to Any Arbitrary Substrate. *ACS Nano* **2013**, *7* (10), 8809−8815.
(67) Ji, Q.; Zhang, Y.; Zhang, Y.; Liu, Z. Chemical Vapour Deposition of Group-VIB Metal Dichalcogenide Monolayers: Engineered Substrates from Amorphous to Single Crystalline. *Chem. Soc. Rev.* **2015**, *44* (9), 2587−2602.
(68) Najmaei, S.; Amani, M.; Chin, M. L.; Liu, Z.; Birdwell, A. G.; O'Regan, T. P.; Ajayan, P. M.; Dubey, M.; Lou, J. Electrical Transport Properties of Polycrystalline Monolayer Molybdenum Disulfide. *ACS Nano* **2014**, *8* (8), 7930−7937.
(69) Geim, A. K.; Grigorieva, I. V. Van Der Waals Heterostructures. *Nature* **2013**, *499* (7459), 419−425.
(70) Choudhary, K.; Tavazza, F. Discovery and Characterization of 2D Materials and Their Heterostructures. *2D Nanoscale Heterostruct. Mater. Synth. Prop. Appl.* **2020**, 1.
(71) Wu, R. J.; Odlyzko, M. L.; Mkhoyan, K. A. Determining the Thickness of Atomically Thin MoS2 and WS2 in the TEM. *Ultramicroscopy* **2014**, *147*, 8−20.
(72) Dumcenco, D.; Ovchinnikov, D.; Marinov, K.; Lazic, P.; Gibertini, M.; Marzari, N.; Sanchez, O. L.; Kung, Y.-C.; Krasnozhon, D.; Chen, M.-W.; et al. Large-Area Epitaxial Monolayer MoS 2. *ACS Nano* **2015**, *9* (4), 4611−4620.

https://doi.org/10.1021/acsami.2c03471
ACS Appl. Mater. Interfaces 2022, 14, 18835−18844